


Cite this: *RSC Adv.*, 2023, 13, 8227

Interfacial S–O bonds specifically boost Z-scheme charge separation in a $\text{CuInS}_2/\text{In}_2\text{O}_3$ heterojunction for efficient photocatalytic activity†

Xiaofei Fu,^a Junwu Tao,^a Zizhou Zhao,^a Siwen Sun,^a Lin Zhao,^a Zuming He,^b Yong Gao^a and Yongmei Xia^c

Reducing the recombination rate of photoexcited electron–hole pairs is always a great challenging work for the photocatalytic technique. In response to this issue, herein, a novel Z-scheme $\text{CuInS}_2/\text{In}_2\text{O}_3$ with interfacial S–O linkages was synthesized by a hydrothermal and subsequently annealing method. The Fourier transform infrared (FT-IR) and X-ray photoelectron spectrometer (XPS) measurements confirmed the formation of covalent S–O bonds between CuInS_2 and In_2O_3 . The quenching and electron spin resonance (ESR) tests revealed the Z-scheme transfer route of photogenerated carriers over the $\text{CuInS}_2/\text{In}_2\text{O}_3$ heterojunctions, which was further verified theoretically *via* density functional theory (DFT) calculations. As expected, the $\text{CuInS}_2/\text{In}_2\text{O}_3$ heterojunctions showed significantly boosted photocatalytic activities for lomefloxacin degradation and $\text{Cr}(\text{vi})$ reduction under visible light illumination compared with the bare materials. Accordingly, a synergistic photocatalytic mechanism of Z-scheme heterostructures and interfacial S–O bonding was proposed, in which the S–O linkage could act as a specific bridge to modify the Z-scheme manner for accelerating the interfacial charge transmission. Furthermore, the $\text{CuInS}_2/\text{In}_2\text{O}_3$ heterojunction also exhibited excellent performance perceived in the stability and reusability tests. This work provides a new approach for designing and fabricating novel Z-scheme heterostructures with a high-efficiency charge transfer route.

Received 4th January 2023
Accepted 6th March 2023

DOI: 10.1039/d3ra00043e

rsc.li/rsc-advances

1. Introduction

Along with the rapid development of modern industries like the pharmaceutical, chemical and manufacturing industries, abundant concomitant pollutants like antibiotics and heavy metals have entered into the aquatic ecosystem, posing a severe threat to the environment and human health.^{1–3} In order to alleviate these environmental issues, various water purification technologies, such as adsorption,⁴ ion exchange,⁵ membrane separation,⁶ photocatalysis⁷ and electrocatalysis,⁸ have been studied and applied to remove the aqueous contaminants. Among them, semiconductor-based photocatalysis has become a research hotspot in water environment treatment due to its sustainable, eco-friendly and low-cost characteristics.^{9–11} To date, multitudinous semiconductors have been developed, and typically, semiconducting metallic oxides such as TiO_2 ,¹² ZnO ¹³ and SnO_2 ,¹⁴ are extensively

researched because of their excellent physical and chemical properties. Nevertheless, due to their wide band gap energies, the effective light response is normally restrained to the ultraviolet region, making them less active under visible-light. Thus, seeking an effective visible-light-responsive semiconductor is of great significance in the practical application of photocatalysis.

Indium oxide (In_2O_3), as a typical n-type semiconductor, has been considered as a promising visible-light-active photocatalyst due to its relative narrow band gap (~ 2.7 eV), environmental stability and low toxicity.^{15,16} However, a major shortcoming on the pure In_2O_3 is its high recombination rate of photoinduced charge carries, which has seriously inhibited its photocatalytic activity.¹⁷ To address this drawback, combining In_2O_3 with another semiconductor to form a heterojunction has been regarded as an effective approach to favor the charge separation.¹⁸ In particular, the Z-scheme heterojunction, inspired by the natural photosynthesis, has sparked great interest from researchers due to its efficient carries transfer pattern and the relative higher redox capacity in comparison with the conventional type II heterostructure.^{19–22} For instance, Wang *et al.* fabricated a Z-scheme $\text{In}_2\text{O}_3/\text{CdS}$ photocatalyst and this heterojunction possessed outstanding degradation performance for the doxycycline hydrochloride and levofloxacin owing to the high charge separation rate.²³ Duan and coworkers constructed a $\text{ZnO}/\text{In}_2\text{O}_3$ Z-scheme heterojunction which showed

^aSchool of Resources and Environmental Engineering, Jiangsu University of Technology, Changzhou, 213001, China. E-mail: fuxiaofei@jsut.edu.cn

^bSchool of Microelectronics and Control Engineering, Changzhou University, Changzhou, 213164, China

^cSchool of Materials and Engineering, Jiangsu University of Technology, Changzhou, 213001, China

† Electronic supplementary information (ESI) available. See DOI: <https://doi.org/10.1039/d3ra00043e>


superior photocatalytic performance for H_2 production.²⁴ Recently, copper indium disulfide (CuInS_2), a ternary chalcogenide semiconductor, has shown great potential in photocatalysis due to its narrow band energy (~ 1.8 eV) and high optical absorption coefficient ($\alpha > 10^5 \text{ cm}^{-1}$).^{25,26} Furthermore, the CuInS_2 possesses a theoretically suitable band structures and Fermi levels with those of In_2O_3 ,^{27,28} which makes them prospective candidates for constructing a Z-scheme heterostructure. However, to the best of our knowledge, very few reports currently focus on the assembling of such $\text{CuInS}_2/\text{In}_2\text{O}_3$ composite to achieve a promoted photocatalytic activity.

In general, simple combining of hybridized semiconductors may cause interfacial resistance at their contact regions, which would impede the charge transfer and severely affect their photocatalytic performance.²⁹ To overcome this issue, heterostructures with interfacial bonds were fabricated and the formed intimate linkage was considered to be efficient to accelerate the spatial carrier transportation.^{30,31} For example, Shehzad *et al.* reported that the chemical bonded TiO_2 -graphene displayed high photocatalytic activity attributing to the interfacial Ti–O–C bonds and promoted transfer of electrons.³² In Chen and Jiang's report, the covalently bonded $\text{Bi}_2\text{O}_3/\text{Bi}_2\text{WO}_6$ composite by cosharing of the Bi–O tetrahedron showed superior photocatalytic activities for CO_2 reduction and degradation of RhB.³³ Recently, some researchers have found that calcination treatment on sulphide semiconductors could promote the production of sulfur vacancies, which could delocalize local electrons and contribute to developing the heterogeneous interfaces with chemical bonding.^{29,34} Accordingly, for the $\text{CuInS}_2/\text{In}_2\text{O}_3$ heterojunction, annealing of its precursor in the preparation process may be a prospective method to generate the interfacial chemical linkages between CuInS_2 and In_2O_3 , which would be a key factor to boost its photocatalytic activity.

In this study, a chemically bonded $\text{CuInS}_2/\text{In}_2\text{O}_3$ composite was successfully synthesized using a hydrothermal method followed by annealing treatment. The obtained heterojunction between CuInS_2 and In_2O_3 was formed *via* interfacial S–O linkages verified by the FT-IR and XPS. Besides, we selected lomefloxacin and Cr(vi) as the target contaminants to probe the visible-light photocatalytic performance on the prepared catalysts. Furthermore, a Z-scheme charge separation route was revealed by the quenching and ESR tests, and confirmed theoretically by DFT calculations. Finally, a synergistically enhanced photocatalytic mechanism of Z-scheme heterostructure and interfacial S–O bond on $\text{CuInS}_2/\text{In}_2\text{O}_3$ was proposed and discussed.

2. Experimental

2.1 Chemical materials

Cuprous chloride (CuCl), indium chloride tetrahydrate ($\text{InCl}_3 \cdot 4\text{H}_2\text{O}$), indium nitrate pentahydrate ($\text{In}(\text{NO}_3)_3 \cdot 5\text{H}_2\text{O}$), urea ($\text{CO}(\text{NH}_2)_2$), *N,N*-dimethylformamide, thioacetamide ($\text{C}_2\text{H}_5\text{NS}$), anhydrous ethanol, ammonium oxalate (AO), dimethyl sulfoxide (DMSO), isopropyl alcohol (IPA), and benzoquinone (BQ) were obtained from Sinopharm Chemical Reagent Co., Ltd. (China). The lomefloxacin (LOM) was purchased from Aladdin Chemistry Co., Ltd (China). Besides, the potassium dichromate

($\text{K}_2\text{Cr}_2\text{O}_7$) was supplied by Shiyi Chemical Co., Ltd. (China). All chemicals and reagents are of analytical grade and used directly in the experiment.

2.2 Preparation of CuInS_2 sample

The bare CuInS_2 catalyst was synthesized by a solvothermal method. Typically, 0.3 mmol CuCl and 0.3 mmol $\text{InCl}_3 \cdot 4\text{H}_2\text{O}$ was dissolved and stirred in 40 mL of *N,N*-dimethylformamide to form a mixed solution. Subsequently, 3 mmol of thioacetamide was added into the above mixture under continuous stirring for another 60 min. Then, the obtained homogeneous solution was sealed in a 100 mL teflon-lined stainless autoclave and thermally treated at 180 °C for 16 h. After cooling to the ambient temperature naturally, the precipitate was harvested *via* centrifugation and washed alternately with deionized water and anhydrous ethanol for six times, and then dried in a vacuum oven at 60 °C for 24 h.

2.3 Preparation of $\text{CuInS}_2/\text{In}_2\text{O}_3$ composites

The $\text{CuInS}_2/\text{In}_2\text{O}_3$ photocatalysts with different mass ratios were prepared *via* a solvothermal and followed calcination route. In a typical procedure, 4 mmol $\text{In}(\text{NO}_3)_3 \cdot 5\text{H}_2\text{O}$ and 30 mmol urea were introduced into 50 mL of deionized water with vortex stirring for 20 min, and then a predetermined amount of as-synthesized CuInS_2 was dispersed into the mixed solution with magnetic stirring for 90 min. Afterwards, the obtained suspension was transferred to a teflon-lined stainless autoclave (100 mL) and maintained at 140 °C for 12 h. The resultant product was separated by centrifugation and washed for several times with deionized water and anhydrous ethanol, and then dried at 80 °C for 24 h. Subsequently, the obtained power was calcined at 400 °C for 120 min in a ceramic crucible with a ramp rate of 10 °C min^{-1} under argon atmosphere. The as-prepared $\text{CuInS}_2/\text{In}_2\text{O}_3$ samples with nominal mass ratio 5%, 11%, 17% and 23% CuInS_2 were denoted as 5- $\text{CuInS}_2/\text{In}_2\text{O}_3$, 11- $\text{CuInS}_2/\text{In}_2\text{O}_3$, 17- $\text{CuInS}_2/\text{In}_2\text{O}_3$, and 23- $\text{CuInS}_2/\text{In}_2\text{O}_3$, respectively. For comparison, the pure In_2O_3 was prepared *via* the similar procedure only without the introduction of CuInS_2 .

2.4 Characterization and theoretical calculation

The details about characterization and theoretical calculation on the fabricated materials were provided in the ESI† SM1.

2.5 Photocatalytic activity evaluation

The photocatalytic performance of the synthesized catalysts were investigated through degrading lomefloxacin (LOM) and reducing Cr(vi) under visible light irradiation. The typical photocatalytic test was conducted as follows: 200 mg of each as-synthesized material was dispersed into 500 mL LOM (30 mg L^{-1}) or Cr(vi) (50 mg L^{-1}) aqueous solution under continuous stirring. To ensure the adsorption–desorption equilibrium, the suspension was vigorously stirred in dark for 30 min. Afterwards, the reaction system was irradiated by a 350 W Xe-lamp (CEL-HXUV500, CEAULIGHT, Beijing, China) equipped with a 420 nm cut-off filter, and 5 mL of the



suspensions were sucked out at timed intervals and immediately centrifuged for the removal of catalyst powders. The concentrations of residual LOM were determined by an UV-vis spectrophotometer (TU-1900) at a wavelength of 286 nm, and the remaining Cr(vi) concentrations were measured colorimetrically at 540 nm with the standard diphenylcarbazide method. All the experimental data were the average of three duplicate determinations.

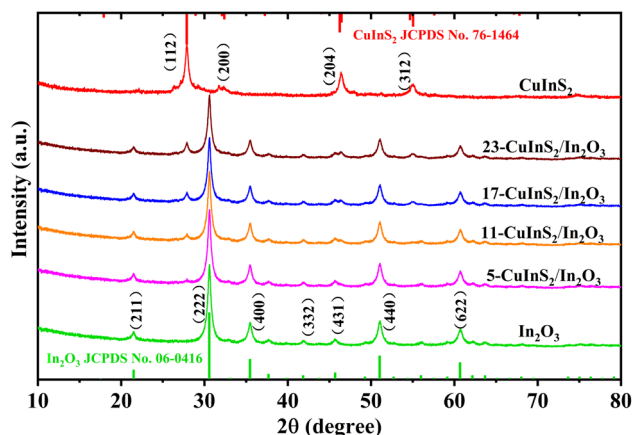


Fig. 1 XRD patterns recorded on bare In_2O_3 , CuInS_2 and $\text{CuInS}_2/\text{In}_2\text{O}_3$ composites.

3. Results and discussion

3.1 XRD analysis

The crystalline phase and purity of all prepared catalysts were characterized by XRD measurements, and the results are shown in Fig. 1. In the XRD pattern of bare In_2O_3 , the diffraction peaks at 21.5°, 30.6°, 35.5°, 41.8°, 45.7°, 51.0° and 60.7° could be assigned to the (211), (222), (400), (332), (431), (440) and (622) crystal planes of cubic phase In_2O_3 (JCPDS no. 06-0416), respectively.³⁵ For bare CuInS_2 , the typical peaks located at 27.8°, 32.4°, 46.2° and 55.0° were observed, which corresponded well to the (112), (200), (204) and (312) crystal reflections of CuInS_2 , respectively (JCPDS no. 76-1461).³⁶ In regard to the $\text{CuInS}_2/\text{In}_2\text{O}_3$ samples, the characteristic peaks of both In_2O_3 and CuInS_2 were identified and no other diffraction peaks of impurities could be observed. At the same time, the peak intensities of CuInS_2 became correspondingly more intense with the CuInS_2 content increasing, and not much difference was observed in the In_2O_3 diffraction peaks. The XRD characterization suggested that CuInS_2 was successfully coupled with In_2O_3 , and their original crystal phases were remained well during the combining process.

3.2 Micromorphology and element analysis

The surface morphologies of as-prepared In_2O_3 , CuInS_2 and 17- $\text{CuInS}_2/\text{In}_2\text{O}_3$ composite were depicted by SEM and TEM. As

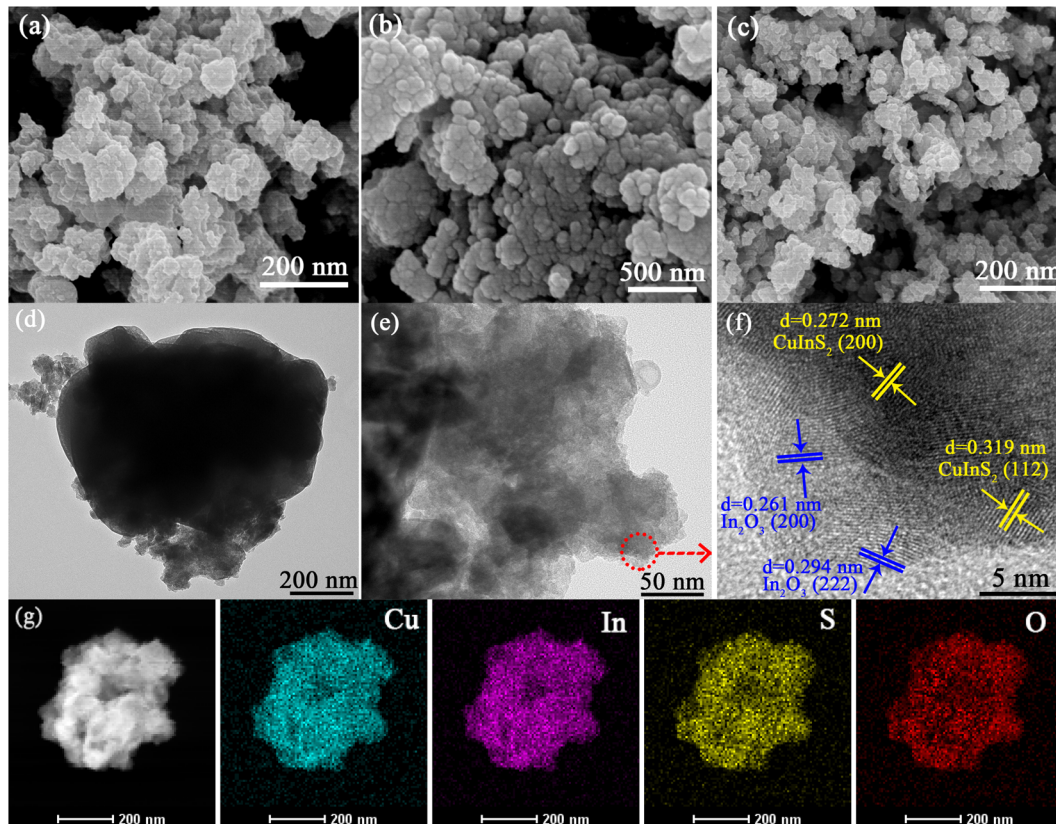


Fig. 2 SEM images of (a) In_2O_3 , (b) CuInS_2 and (c) 17- $\text{CuInS}_2/\text{In}_2\text{O}_3$ sample; TEM images (d, e) and HRTEM image (f) of 17- $\text{CuInS}_2/\text{In}_2\text{O}_3$; (g) HAADF-STEM image and corresponding EDS elemental mappings of 17- $\text{CuInS}_2/\text{In}_2\text{O}_3$.

displayed in Fig. 2(a), the bare In_2O_3 presented stacked small-size plate structure. In Fig. 2(b), it was observed that the pure CuInS_2 was constructed by dense nanoparticles with concomitant aggregation. For 17- $\text{CuInS}_2/\text{In}_2\text{O}_3$ composite, it was found that the lamellar In_2O_3 and CuInS_2 particles were both in its morphology (Fig. 2(c)). Besides, to further investigate the detailed information of the morphology and crystal structure, TEM and HRTEM analysis on 17- $\text{CuInS}_2/\text{In}_2\text{O}_3$ were carried out. As illustrated in Fig. 2(d and e), there was intimate interface contact between In_2O_3 and CuInS_2 . In addition, the HRTEM image clearly showed the lattice fringes of the two substances. Among, the interplanar spacings of 0.272 and 0.319 nm corresponded to the (200) and (112) crystal planes of CuInS_2 ,^{36,37} and the spacings of the 0.261 and 294 nm were attributed to the (200) and (222) planes of In_2O_3 ,^{16,38} respectively, which was in good agreement with the results from XRD analysis. Moreover, the high-angle annular dark field (HAADF) image and corresponding element mapping of 17- $\text{CuInS}_2/\text{In}_2\text{O}_3$ (Fig. 2(f)) demonstrated the presence of Cu, In, S and O elements, further testifying the co-existing of both CuInS_2 and In_2O_3 in this composite.

3.3 FT-IR and XPS analysis

The FT-IR spectra were performed to explore the structure and bond characteristics of the as-prepared samples. As observed in Fig. 3, the FT-IR spectrum recorded on bare In_2O_3 revealed the In–O stretching vibrations at 426 and 560 cm^{-1} and the In–O bending vibration at 604 cm^{-1} .^{27,35} In addition, the bands centered at 3456 and 1592 cm^{-1} could be ascribed to the stretching and bending vibration of –OH groups from physical adsorbed water, respectively.³⁹ In the FT-IR spectrum of bare CuInS_2 , the bands at 1700 and 1449 cm^{-1} belonged to the S–In and S–Cu vibrations, respectively.^{40,41} For the composite of 17- $\text{CuInS}_2/\text{In}_2\text{O}_3$, all the typical bands of surface bonds on In_2O_3 and CuInS_2 were detected, suggesting their coexistence in this composite. Of note, a new band located at 1061 cm^{-1} was observed, which could be assigned to the vibration of S–O bond.²⁹ This S–O bond might be formed *via* the reaction of the

unsaturated S vacancies in CuInS_2 and O atoms in In_2O_3 , suggesting the construction of interfacial linkages in $\text{CuInS}_2/\text{In}_2\text{O}_3$ heterostructure.

The XPS determination was used to probe more details about the surface element composition and chemical states on the as-synthesized catalysts. As depicted in Fig. 4(a), the In 3d spectrum for bare In_2O_3 was divided into two symmetrical peaks at 452.2 and 444.6 eV, corresponding to In 3d_{3/2} and 3d_{5/2}, respectively.²⁹ The energy peaks of Cu 2p_{1/2} and 2p_{3/2} on bare CuInS_2 were located at 950.2 and 930.8 eV,⁴² respectively (Fig. 4(b)). While for the 17- $\text{CuInS}_2/\text{In}_2\text{O}_3$ composite, the In 3d energy positions were observed to shift to lower states (Fig. 4(a)), and meanwhile the Cu 2p states showed a positive shift (Fig. 4(b)) in comparison with the individual materials. Fig. 4(c) presents the high resolution XPS spectra of S 2p on bare CuInS_2 and 17- $\text{CuInS}_2/\text{In}_2\text{O}_3$ sample. The S 2p spectrum on bare CuInS_2 could be decomposed into two peaks at 163.1 eV (S–In) and 161.9 eV (S–Cu), respectively.⁴³ In the case of 17- $\text{CuInS}_2/\text{In}_2\text{O}_3$ composite, the fitted S 2p peaks of S–In (163.6 eV) and S–Cu (162.4 eV) exhibited a positive shift, and notably, a new peak was observed at 164.6 eV associated with the S–O bonds.^{29,34} In Fig. 4(d), the fitting curve of O 1s on bare In_2O_3 involved two peaks at 532.6 and 529.8 eV, which were ascribed to the –OH from surface adsorbed water and In–O–In bond in the structure of In_2O_3 , respectively.¹⁶ Furthermore, an additional peak was developed at 531.6 eV in the O 1s spectrum of 17- $\text{CuInS}_2/\text{In}_2\text{O}_3$ composite, which could corresponded to the S–O bonds.^{29,44} According to the above fitting results, it was found that each element in 17- $\text{CuInS}_2/\text{In}_2\text{O}_3$ showed a negative or positive shift in the banding energy compared with that of bare materials as indicated in Fig. 4(a–d), and moreover, the formation of interfacial S–O bonds was testified by XPS measurement in consistency with the results from FT-IR, indicating the intimate interfacial contact between CuInS_2 and In_2O_3 .

3.4 UV-vis DRS analysis

UV-vis diffuse reflectance spectra (DRS) were recorded for investigating the photo-response range on the prepared photocatalysts. As displayed in Fig. 5(a), the optical absorption edge of bare In_2O_3 was found at approximate 500 nm. After combining with CuInS_2 , the $\text{CuInS}_2/\text{In}_2\text{O}_3$ composites revealed gradually promoted visible light response in the range of 500–800 nm with the CuInS_2 loading content increasing, which was attributed to the excellent light absorption on CuInS_2 . In addition, the band gap energies of the bulk CuInS_2 and In_2O_3 was analyzed *via* the following equation:⁴⁵ $\alpha h\nu = A(h\nu - E_g)^{n/2}$, in which α and A represent the absorption coefficients, h , ν and E_g stand for the Planck constant, light frequency and band gap energy, respectively, and n depends on the transition feature of electrons in the semiconductor with 1 and 4 for a direct transition and indirect transition gap one, respectively. In this case, both CuInS_2 and In_2O_3 were disclosed to reveal direct transitions.^{27,41} Accordingly, the band gap values of CuInS_2 , In_2O_3 , 5- $\text{CuInS}_2/\text{In}_2\text{O}_3$, 11- $\text{CuInS}_2/\text{In}_2\text{O}_3$, 17- $\text{CuInS}_2/\text{In}_2\text{O}_3$ and 23- $\text{CuInS}_2/\text{In}_2\text{O}_3$ were estimated to be 1.81, 2.75, 2.73, 2.70, 2.67 and 2.62 eV, respectively (Fig. 5(b)).

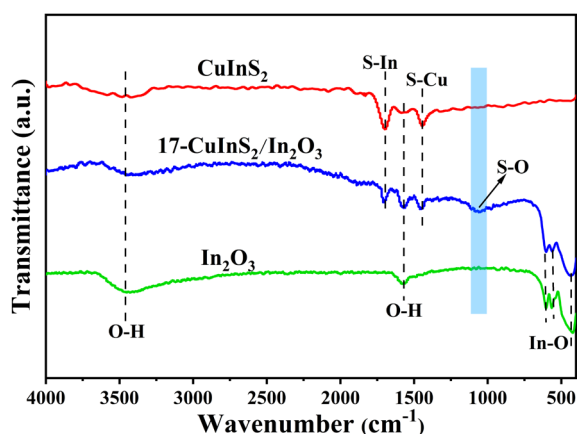


Fig. 3 FT-IR spectra of bare In_2O_3 , CuInS_2 and 17- $\text{CuInS}_2/\text{In}_2\text{O}_3$ composite.



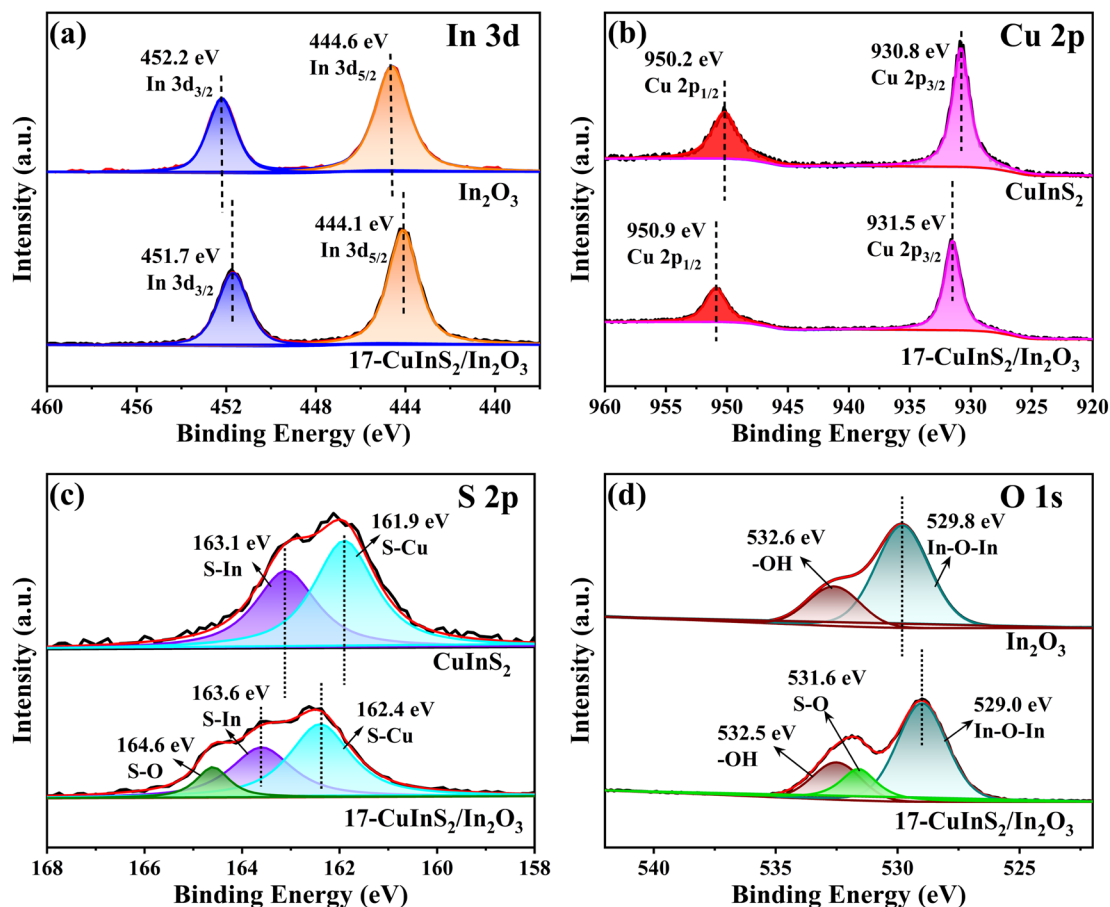


Fig. 4 High-resolution XPS spectra of (a) In 3d, (b) Cu 2p, (c) S 2p, and (d) O 1s on bare In₂O₃, CuInS₂ and 17-CuInS₂/In₂O₃ composite.

3.5 Photoluminescence and photocurrent analysis

The photoluminescence (PL) emission spectra were used to explore the recombination rate of photoinduced electrons and holes on the prepared photocatalysts. As illustrated in Fig. 6(a), the CuInS₂/In₂O₃ samples exhibited obviously declining PL emission intensities in comparison with the pure In₂O₃ and CuInS₂, indicated that the recombination of charge carriers was effectively restrained in the composites.^{46,47} In addition, it was

found that the loading content of CuInS₂ in the composites had a great influence on the PL intensity. Notably, the 17-CuInS₂/In₂O₃ possessed the lowest PL emission intensity, implying its highest separation efficiency of electron-hole pairs in the photocatalytic process. Furthermore, to confirm the charge separation efficiency on the obtained catalysts, photocurrent response tests were carried out and the results are shown in Fig. 6(b). Normally, the higher photocurrent intensity indicates

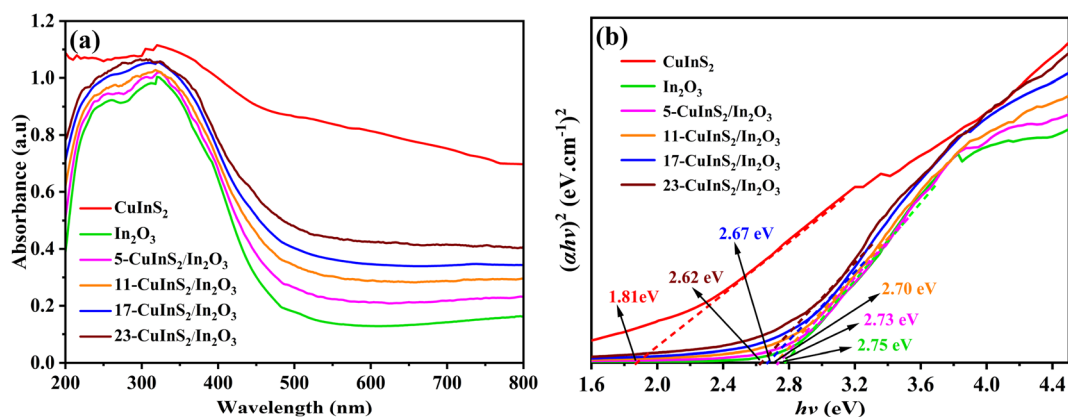


Fig. 5 (a) UV-vis DRS spectra of different samples and (b) Plots of $(ah\nu)^2$ versus $h\nu$ on pure CuInS₂ and In₂O₃.

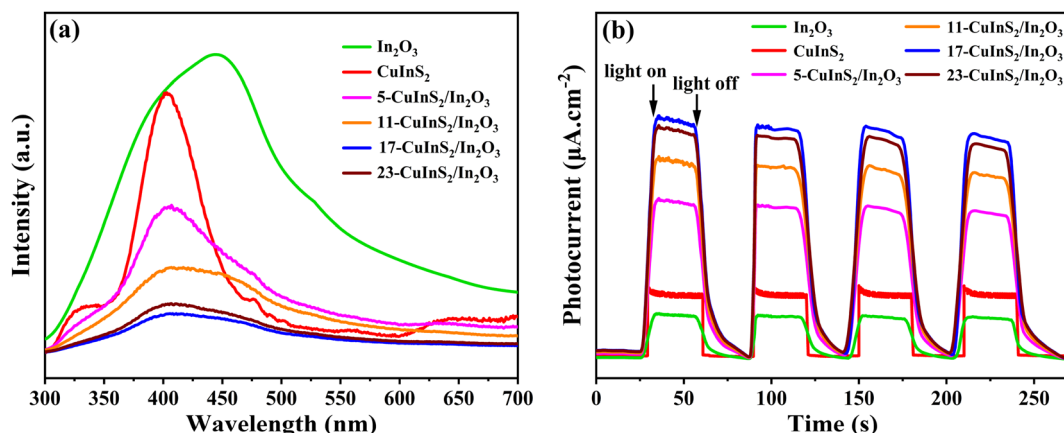


Fig. 6 Photoluminescence spectra (a) and photocurrent density curves (b) on bare In₂O₃, CuInS₂ and CuInS₂/In₂O₃ composites.

the larger charge transfer and separation rate on the semiconductor.^{48,49} It was observed that the CuInS₂/In₂O₃ composites displayed enhanced photocurrent response densities compared to the bare materials, and the 17-CuInS₂/In₂O₃ showed the strongest response density, suggesting the outstanding charge separation efficiency inside 17-CuInS₂/In₂O₃. This result was kept in line with the analysis of PL

spectra, which might be due to the tight interfacial contact with covalent S–O bonds between CuInS₂ and In₂O₃.

3.6 Photocatalytic activity

Photocatalytic experiments of degrading LOM and reducing Cr(vi) conducted under visible light irradiation were used to evaluate the photocatalytic performance of the as-fabricated

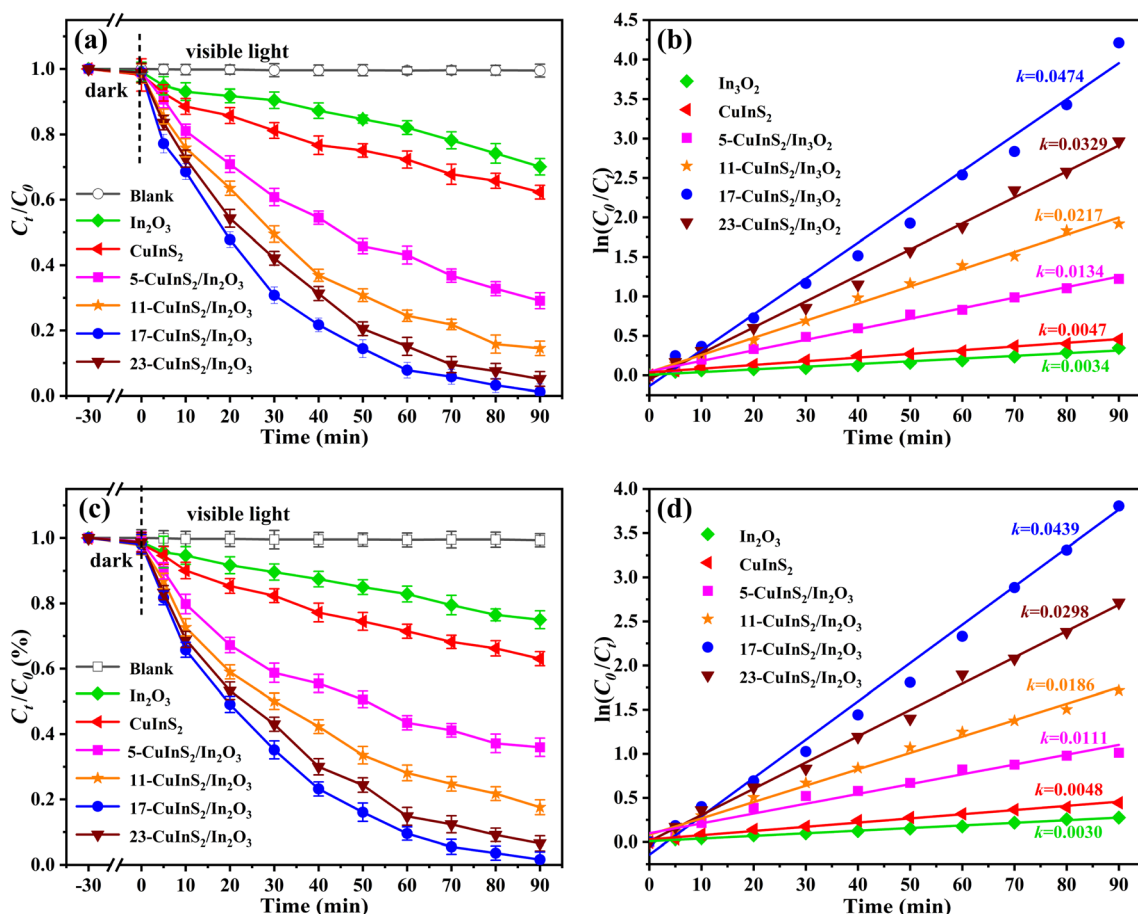


Fig. 7 Photocatalytic degradation of LOM (a) and reduction of Cr(vi) (c), with (b) and (d) the corresponding pseudo-first-order kinetics on the as-prepared photocatalysts under visible light irradiation.



photocatalysts. In addition, the blank tests were also carried out to estimate the photostability of the selected pollutants under light irradiation. Fig. 7(a) presents the photo-degradation activities of different samples towards LOM solution. It could be found that there was very little degradation rate of LOM with direct photolysis (without solids), suggesting the tenacious stability of aqueous LOM. Besides, after the addition of bare In_2O_3 , only 29.9% of LOM was degraded in 90 min, and meanwhile the pure CuInS_2 also displayed unsatisfactory photocatalytic performance with 37.7% LOM degradation rate. By contrast, all the $\text{CuInS}_2/\text{In}_2\text{O}_3$ composites showed boosted photocatalytic activities. Among them, the 17- $\text{CuInS}_2/\text{In}_2\text{O}_3$ possessed the highest photo-degradation rate of LOM (98.8%) after 90 min visible light irradiation, which might mainly due to its excellent separation efficiency of electron-hole pairs demonstrated by the PL and photocurrent measurements. Additionally, the photo-reaction kinetics of LOM over different catalysts were analyzed *via* the pseudo-first order kinetic formula ($\ln(C_0/C_t) = kt$).⁵⁰ As illustrated in Fig. 7(b), the fitted curves were in good accordance with the kinetic model, and the 17- $\text{CuInS}_2/\text{In}_2\text{O}_3$ revealed the fastest rate constant (0.0474 min^{-1}), which was 10.1 and 13.9 times higher than that of bare CuInS_2 (0.0047 min^{-1}) and In_2O_3 (0.0034 min^{-1}), respectively.

Fig. 7(c) shows the photocatalytic performance for $\text{Cr}(\text{vi})$ reduction on the prepared catalysts. Similar to the LOM degradation, the removal rate of $\text{Cr}(\text{vi})$ was almost negligible in the blank experiment. Besides, both bare CuInS_2 and In_2O_3 presented low catalytic performance with only 37.1% and 25.2% reduction rate of $\text{Cr}(\text{vi})$, respectively. However, markedly improved activities of $\text{CuInS}_2/\text{In}_2\text{O}_3$ were acquired for the removal of $\text{Cr}(\text{vi})$, and in line with the LOM degradation tests, the 17- $\text{CuInS}_2/\text{In}_2\text{O}_3$ also displayed the best reduction rate of $\text{Cr}(\text{vi})$ (98.1%) in the 90 min reaction time. Furthermore, the obtained rate constants resulted from the pseudo-first order kinetic curves disclosed that the k value on the 17- $\text{CuInS}_2/\text{In}_2\text{O}_3$ (0.0439 min^{-1}) was 9.14 and 14.6 times higher than that of pure CuInS_2 (0.0048 min^{-1}) and In_2O_3 (0.0030 min^{-1}), respectively (Fig. 7(d)). In addition, the photocatalytic activity of the 17- $\text{CuInS}_2/\text{In}_2\text{O}_3$ composite was also compared with those of other reported photocatalysts. As displayed in Table S1,[†] the 17-

$\text{CuInS}_2/\text{In}_2\text{O}_3$ showed a quite competitive performance in the photocatalytic removal of lomefloxacin and $\text{Cr}(\text{vi})$.

The cyclic stability of the 17- $\text{CuInS}_2/\text{In}_2\text{O}_3$ photocatalyst was evaluated *via* the consecutive LOM degradation and $\text{Cr}(\text{vi})$ reduction for five times, respectively. As can be obtained from Fig. 8(a), the photocatalytic performance of 17- $\text{CuInS}_2/\text{In}_2\text{O}_3$ had no obvious deactivation with only 2.8% and 3.6% decline in LOM degradation and $\text{Cr}(\text{vi})$ reduction after five runs, respectively, disclosing its remarkable reusability. Besides, it could be concluded from the XRD patterns (Fig. 8(b)) and S 2p and O 1s XPS spectra (Fig. S1[†]) of 17- $\text{CuInS}_2/\text{In}_2\text{O}_3$ before and after five cycles that its crystal structure basically remained unchanged during the reactions, which further verifying its chemical stability.

3.7 Mechanism analysis

In order to elucidate the photocatalytic mechanism on the as-synthesized materials, density functional theory (DFT) calculation was used to explore the electronic band structures of bulk CuInS_2 and In_2O_3 . As presented in Fig. 9(a and b), the direct band gaps of the CuInS_2 and In_2O_3 were calculated to be 1.77 and 2.71 eV, respectively, which were very close to the Tauc plot results of 1.81 eV (CuInS_2) and 2.75 eV (In_2O_3) from UV-vis DRS spectra (Fig. 5(b)). In addition, the Mott-Schottky (M-S) tests were performed to determine the band potentials of the CuInS_2 and In_2O_3 . As can be seen from the M-S plots (Fig. 9(c and d)), these two materials both belonged to the n-type semiconductors, and the flat band potentials on the CuInS_2 and In_2O_3 were obtained as -0.67 and $-0.19 \text{ V vs. Ag/AgCl}$ ($\text{pH} = 6.8$), respectively, and meanwhile their flat band potentials could be converted to be -0.47 and 0.01 V vs. NHE ($E_{\text{NHE}} = E_{\text{Ag/AgCl}} + 0.2 \text{ V}$),⁵¹ respectively. For the n-type semiconductor, the conduction band (CB) potential is normally more negative by approximately 0.1 V than the flat band potential,¹⁰ thus the CB potentials of the CuInS_2 and In_2O_3 were determined to be -0.57 and -0.09 V vs. NHE , respectively. In addition, according to the formula $E_{\text{VB}} = E_{\text{CB}} + E_{\text{g}}$, the corresponding VB potentials were calculated to be 1.24 eV for CuInS_2 and 2.66 eV for In_2O_3 , which agreed well with the results from VB-XPS spectra presented in Fig. S2.[†]

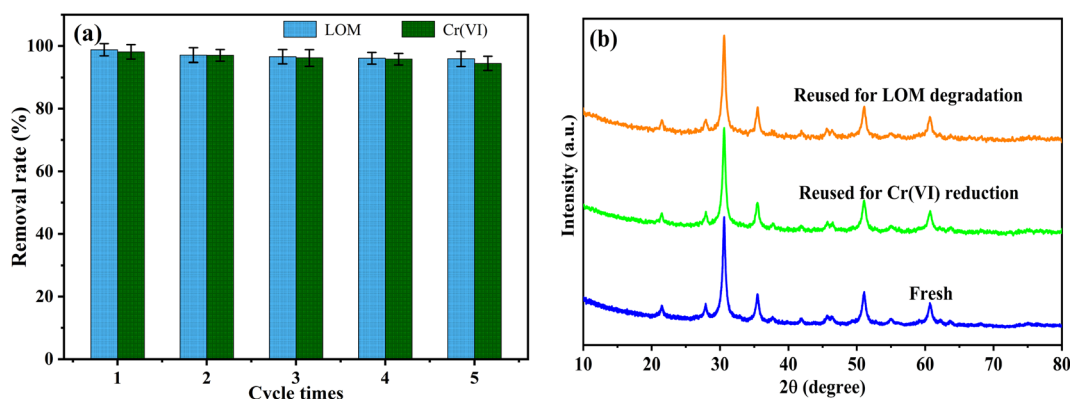


Fig. 8 (a) Recycling experiments of 17- $\text{CuInS}_2/\text{In}_2\text{O}_3$ for LOM degradation and $\text{Cr}(\text{vi})$ reduction, (b) XRD patterns of the fresh and used 17- $\text{CuInS}_2/\text{In}_2\text{O}_3$.

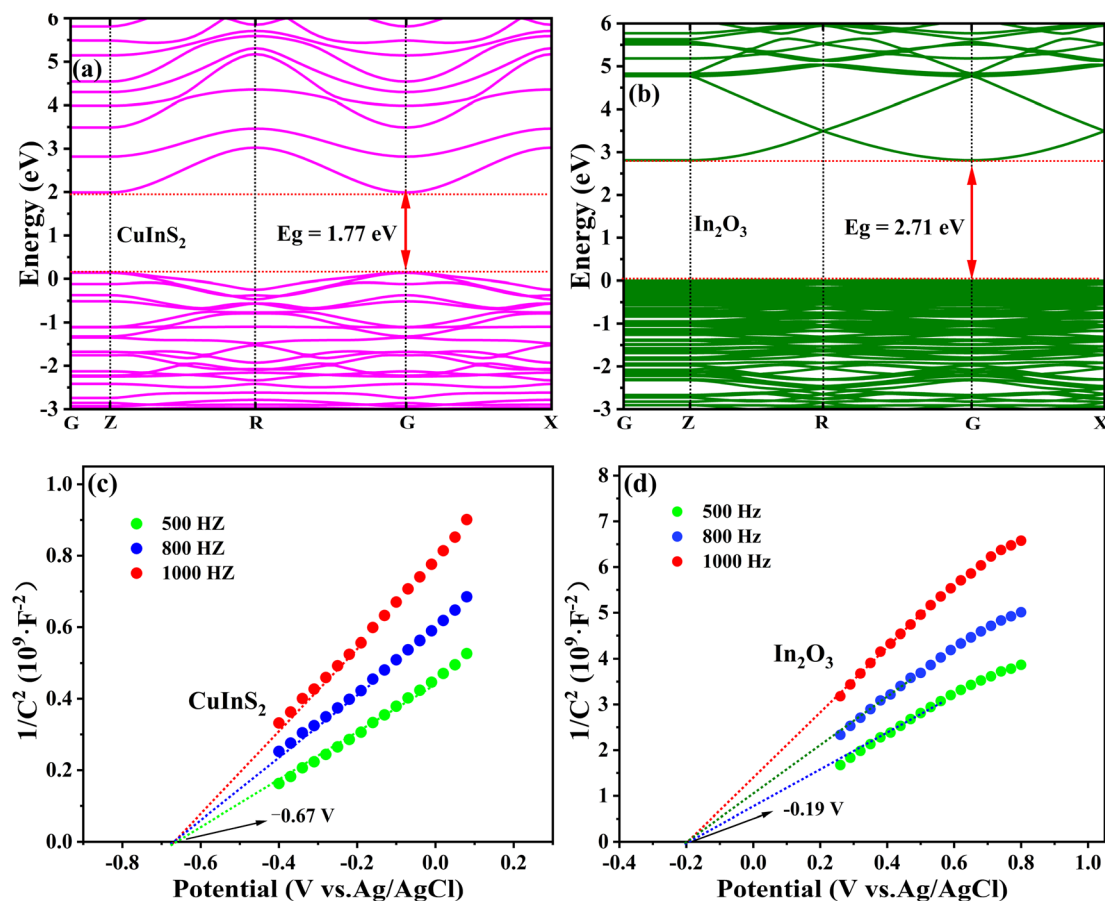


Fig. 9 DFT calculated electronic band structures (a and b) and Mott–Schottky curves (c and d) of CuInS_2 and In_2O_3 .

To clearly clarify the effect of reactive species involving the photocatalytic activity over 17- $\text{CuInS}_2/\text{In}_2\text{O}_3$, quenching tests were carried out by adding ammonium oxalate (AO), dimethyl sulfoxide (DMSO), isopropyl alcohol (IPA) and benzoquinone (BQ) as sacrificial agents for holes (h^+), electrons (e^-), hydroxyl radicals ($\cdot\text{OH}$) and superoxide radicals ($\cdot\text{O}_2^-$), respectively.⁵² As displayed in Fig. 10(a), there was a sharp decline (from 98.8% to 18.6%) in the photo-degradation rate of LOM when the IPA was added as the scavenger, suggesting that $\cdot\text{OH}$ played the key role in degrading LOM. Besides, the introductions of AO and BQ had apparently negative effects on LOM degradation with the degradation rates decreasing to 48.2% and 35.1%, respectively, indicating that the h^+ and $\cdot\text{O}_2^-$ species both played important roles in LOM degradation. For the trapping experiments of $\text{Cr}(\text{vi})$ reduction, it was observed that adding DMSO could significantly restrain the reduction of $\text{Cr}(\text{vi})$ (17.4%), revealing that the photoinduced e^- directly participated in the $\text{Cr}(\text{vi})$ reduction and acted as the dominant role in the reaction. In addition, the $\text{Cr}(\text{vi})$ reduction rate was greatly suppressed in the presence of BQ (30.2%), implying that $\cdot\text{O}_2^-$ radicals also played a crucial role in $\text{Cr}(\text{vi})$ reduction.

Additionally, ESR measurements were conducted to further examine the existence of $\cdot\text{O}_2^-$ and $\cdot\text{OH}$ active species generated in the photocatalytic system. As shown in Fig. 10(b), there was no distinct peak in the absence of light, and the bare In_2O_3 also

displayed no characteristic peak in its ESR spectrum for $\text{DMPO}\cdot\text{O}_2^-$, which could be due to that the induced e^- in the CB of In_2O_3 (-0.09 eV vs. NHE) was not strong enough to reactive with O_2 to generate $\cdot\text{O}_2^-$ ($\text{O}_2/\cdot\text{O}_2^-$, -0.33 eV vs. NHE).⁵³ Meanwhile, four characteristic peaks of $\text{DMPO}\cdot\text{O}_2^-$ were detected on the bare CuInS_2 after 8 min visible light irradiation. Noticeably, the typical signals of $\text{DMPO}\cdot\text{O}_2^-$ were extremely enhanced on the 17- $\text{CuInS}_2/\text{In}_2\text{O}_3$, indicating that abundant O_2^- radicals had been produced in this catalytic system. Fig. 10(c) depicts the ESR spectra of $\text{DMPO}\cdot\text{OH}$ performed on the as-prepared samples. It was found that no characteristic signal could be observed in dark, while four typical peaks of $\text{DMPO}\cdot\text{OH}$ appeared in the ESR spectrum on the bare In_2O_3 , suggesting the existence of $\cdot\text{OH}$ species in the photoreaction. As for the bare CuInS_2 , no obvious peak could be perceived in its ESR curve for $\text{DMPO}\cdot\text{OH}$, on account of the lower oxidation ability of h^+ in the VB of CuInS_2 (1.24 eV vs. NHE) relative to the standard potential of $\text{H}_2\text{O}/\cdot\text{OH}$ (2.4 eV vs. NHE).⁵⁴ However, the 17- $\text{CuInS}_2/\text{In}_2\text{O}_3$ exhibited a significant enhancement of $\text{DMPO}\cdot\text{OH}$ peaks compared with bare In_2O_3 , revealing that the combination of In_2O_3 and CuInS_2 could greatly promote the production of $\cdot\text{OH}$ radicals.

Based on the above band structure analysis of CuInS_2 and In_2O_3 , it was assumed that the 17- $\text{CuInS}_2/\text{In}_2\text{O}_3$ was constructed within a traditional type II band alignment, the photoexcited e^-



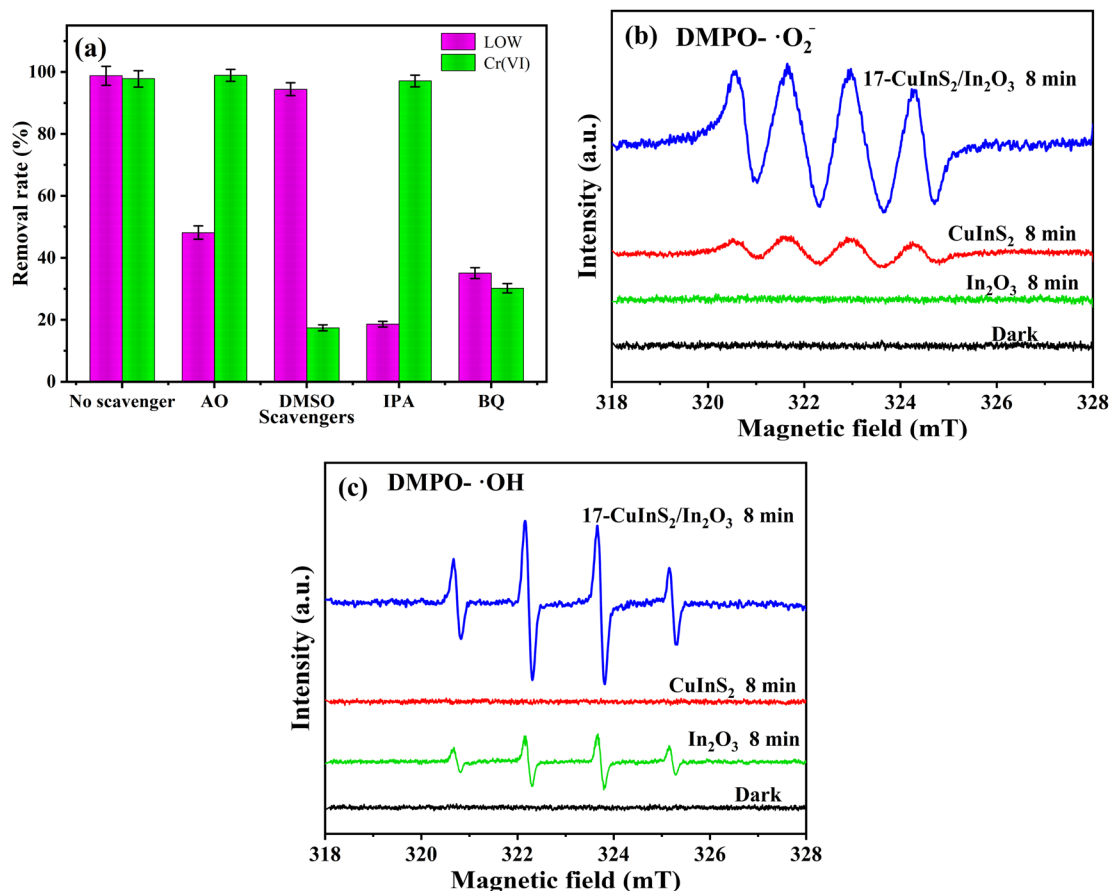


Fig. 10 Photocatalytic removal of LOM and Cr(VI) over 17-CuInS₂/In₂O₃ with different sacrificial agents (a), ESR spectra of $\cdot\text{O}_2^-$ (b) and $\cdot\text{OH}$ (c) radicals trapped by DMPO on 17-CuInS₂/In₂O₃.

in the CB of CuInS₂ (-0.57 eV vs. NHE) should move down to that of In₂O₃ (-0.09 eV vs. NHE), and simultaneously, the generated h^+ in the VB of In₂O₃ (2.66 eV vs. NHE) would transfer to that of CuInS₂ (1.24 eV vs. NHE). Nevertheless, in this case, neither $\cdot\text{O}_2^-$ nor $\cdot\text{OH}$ could be produced in the photocatalytic reactions with 17-CuInS₂/In₂O₃ composite, which be in contradiction to the results from the quenching and ESR tests.

Thereby, the charge transfer mechanism of this CuInS₂/In₂O₃ heterojunction may belong to a Z-scheme pattern. To further testify this supposition and make certain the charge transfer model at interface, work functions of CuInS₂ and In₂O₃ were calculated by the DFT method. As indicated in Fig. 11, the surface work functions (Φ) of CuInS₂ and In₂O₃ were simulated to be 3.28 and 5.76 eV, respectively. According to the formula of

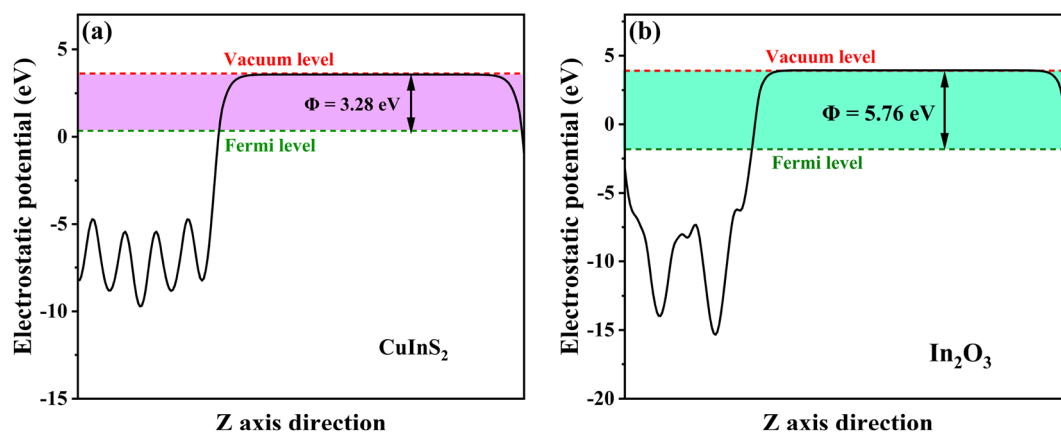


Fig. 11 Calculated work functions of (a) CuInS₂ and (b) In₂O₃.

$E_f = E_{va} - \Phi$,⁵⁵ in which E_f and E_{va} stand for the Fermi level and electrostatic potential of vacuum level, respectively, the Fermi energy of CuInS₂ was higher than that of In₂O₃. Thus, when CuInS₂ and In₂O₃ form an intimate heterostructure, the e^- at the CuInS₂/In₂O₃ interface will be rearranged with a migration from CuInS₂ to In₂O₃ until their Fermi energies attain an equilibrium, and as a result, the internal electric field (IEF) will be formed with the orientation from CuInS₂ to In₂O₃. Thereby, due to the IEF, the photoexcited e^- in In₂O₃ should transfer to CuInS₂ in the 17-CuInS₂/In₂O₃ reaction system, forming the Z-scheme transfer path.

As a whole, the Z-scheme photocatalytic mechanism over CuInS₂/In₂O₃ heterostructure is proposed and illustrated in Fig. 12. Firstly, once the CuInS₂/In₂O₃ was irradiated by the visible light, both CuInS₂ and In₂O₃ were excited to yield electrons and holes in their CB and VB, respectively. Secondly, owing to the formation of IEF, it would drive the photoexcited electrons to move from the CB of In₂O₃ to the VB of CuInS₂ *via* interfacial S–O bonds, and then the recombination of electrons and holes occurred there. In the meantime, the electrons congregated in the CB of CuInS₂ could directly reduce Cr(VI) to Cr(III) or produce $\cdot O_2^-$ *via* reacting with O₂, and subsequently the generated $\cdot O_2^-$ could not only convert Cr(VI) to Cr(III) but also oxidize LOM to smaller molecules. Besides, in the VB of In₂O₃, the accumulated holes would degrade LOM or react with H₂O to produce $\cdot OH$ radicals, further contributing to the degradation of LOM. Based on the aforementioned reaction process, the Z-scheme heterostructure and the formed interfacial S–O bonds between CuInS₂ and In₂O₃ were regarded as the two synergistic factors for the enhanced photocatalytic performance on CuInS₂/In₂O₃ heterojunctions. On the one hand, the built IEF in the Z-scheme heterostructure provided an efficient separate route for e^- – h^+ pairs. On the other hand, the covalent S–O linkage served as a specific bridge to further accelerate the charge separation. By virtue of this synergistic effect, the recombination of e^- – h^+ pairs was markedly suppressed on the CuInS₂/In₂O₃ composite, thus greatly enhancing its photocatalytic performance for aqueous LOM and Cr(VI).

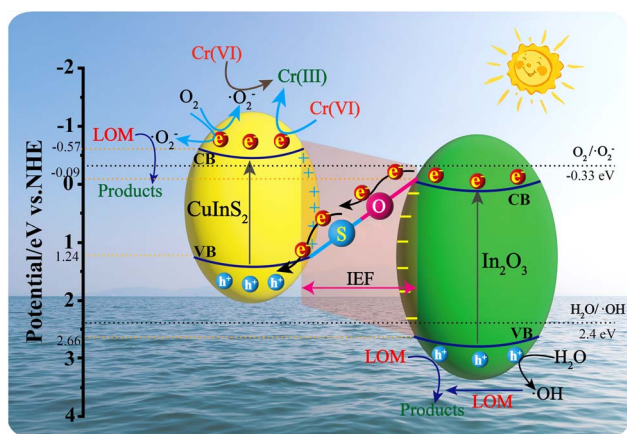


Fig. 12 Schematic representation of proposed photocatalytic mechanism on CuInS₂/In₂O₃ for LOM degradation and Cr(VI) reduction under visible light irradiation.

4. Conclusions

In summary, a covalently bonded CuInS₂/In₂O₃ composite photocatalyst was successfully prepared *via* a hydrothermal and followed annealing route. The synthesized CuInS₂/In₂O₃ heterostructure possessed an intimate interface with covalent S–O bonds confirmed by the FT-IR and XPS characterizations. In addition, the trapping and ESR tests disclosed a Z-scheme charge transfer pattern associated with the CuInS₂/In₂O₃ heterojunction, and this transfer model was further demonstrated theoretically *via* the DFT calculations. As a result, in comparison with the individual materials, the optimal 17-CuInS₂/In₂O₃ composite exhibited extremely promoted photocatalytic performance in degrading LOM and reducing Cr(VI) under visible light irradiation. In this CuInS₂/In₂O₃ system, the built IEF provided an efficient Z-scheme separation path for charge carriers, and meanwhile the formed interfacial S–O bond acted as a bridge to further boost this separation rate. Thus, the Z-scheme heterostructure and S–O linkages showed a synergistic effect for the enhanced photocatalytic activities over CuInS₂/In₂O₃ composites. In addition, the fabricated heterojunctions also presented good stability and reusability in five test cycles. This work provides an innovative route to constructing high-performance Z-scheme photocatalysts for environmental pollution.

Author contributions

Xiaofei Fu: conceptualization, validation, formal analysis, writing-original draft, writing-review & editing. Junwu Tao: formal analysis, visualization, data curation. Zizhou Zhao: formal analysis, methodology, data curation. Siwen Sun: formal analysis, visualization, data curation. Lin Zhao: formal analysis, data curation. Zuming He: investigation, supervision, writing-review & editing. Yong Gao: supervision, formal analysis, visualization, supervision. Yongmei Xia: formal analysis, writing-review & editing. All authors have approved the final version of the manuscript.

Conflicts of interest

There are no conflicts to declare.

Acknowledgements

This work was supported by the Specialized Research Fund for the Doctoral Program of Jiangsu University of Technology (KYY16018) and the Innovation and Entrepreneurship Training Program for Jiangsu college students (202211463073Y).

References

- 1 H. Zhang, L. chao Nengzi, Z. Wang, X. Zhang, B. Li and X. Cheng, *J. Hazard. Mater.*, 2020, **383**, 121236.
- 2 Q. Wu, H. Yang, L. Kang, Z. Gao and F. Ren, *Appl. Catal., B*, 2020, **263**, 118282.



- 3 J. W. Wang, F. G. Qiu, P. Wang, C. Ge and C. C. Wang, *J. Cleaner Prod.*, 2021, **279**, 123408.
- 4 A. M. Ismail, A. A. Menazea and H. Ali, *J. Mater. Sci.: Mater. Electron.*, 2021, **32**, 19352.
- 5 P. Czupryński, M. Plotka, P. Glamowski, W. Żukowski and T. Bajda, *RSC Adv.*, 2022, **12**, 5145–5156.
- 6 C. A. Kozłowski and W. Walkowiak, *Water Res.*, 2002, **36**, 4870–4876.
- 7 L. Kang, Z. Han, H. Yu, Q. Wu and H. Yang, *Sep. Purif. Technol.*, 2022, **278**, 119482.
- 8 J. Han, S. Zhang, Q. Song, H. Yan, J. Kang, Y. Guo and Z. Liu, *Sustainable Energy Fuels*, 2021, **5**, 509–517.
- 9 L. Li, H. Gao, G. Liu, S. Wang, Z. Yi, X. Wu and H. Yang, *Adv. Powder Technol.*, 2022, **33**, 103481.
- 10 S. V. P. Vattikuti, A. K. R. Police, J. Shim and C. Byon, *Appl. Surf. Sci.*, 2018, **447**, 740–756.
- 11 X. Dong, H. Hao, N. Wang, H. Yuan and X. Lang, *J. Colloid Interface Sci.*, 2021, **590**, 387–395.
- 12 J. Juay, J. C. E. Yang, H. Bai and D. D. Sun, *RSC Adv.*, 2022, **12**, 25449.
- 13 Z. He, Y. Xia, B. Tang, X. Jiang and J. Su, *Mater. Lett.*, 2016, **184**, 148–151.
- 14 Y. Lv, Z. Yu, S. Huang, F. Deng, K. Zheng, G. Yang, Y. Liu, C. Lin, X. Ye and M. Liu, *Chemosphere*, 2021, **271**, 129452.
- 15 A. Saroni, M. Alizadeh, S. A. Rahman, W. Meevasana and B. T. Goh, *J. Power Sources*, 2020, **480**, 228829.
- 16 J. Shen, L. Qian, J. Huang, Y. Guo and Z. Zhang, *Sep. Purif. Technol.*, 2021, **275**, 119239.
- 17 S. Wang, B. Y. Guan and X. W. D. Lou, *J. Am. Chem. Soc.*, 2018, **140**, 5037–5040.
- 18 H. Xu, H. Chen, S. Chen, K. Wang and X. Wang, *Int. J. Hydrogen Energy*, 2021, **46**, 32445–32454.
- 19 Y. Wang, F. Xu, L. Sun, Y. Li, L. Liao, Y. Guan, J. Lao, Y. Yang, T. Zhou, Y. Wang, B. Li, K. Zhang and Y. Zou, *RSC Adv.*, 2022, **1**, 541004.
- 20 Z. He, M. S. Siddique, H. Yang, Y. Xia, J. Su, B. Tang, L. Wang, L. Kang and Z. Huang, *J. Cleaner Prod.*, 2022, **339**, 130634.
- 21 Z. He, H. Yang, J. Su, Y. Xia, X. Fu, L. Wang and L. Kang, *Fuel*, 2021, **294**, 120399.
- 22 H. Hao and X. Lang, *ChemCatChem*, 2019, **11**, 1378–1393.
- 23 T. Wang, Z. Zeng, J. Yang, Z. Pan, X. Zheng, Y. Guo and T. Huang, *Colloids Interface Sci. Commun.*, 2022, **51**, 100674.
- 24 Y. Duan, J. Xue, J. Dai, Y. Wei, C. Wu, S. H. Chang and J. Ma, *Appl. Surf. Sci.*, 2022, **592**, 153306.
- 25 X. Fu, J. Tao, Z. He, Y. Gao, Y. Xia and Z. Zhao, *J. Mater. Sci.: Mater. Electron.*, 2022, **33**, 24663–24676.
- 26 H. Tang, Y. Deng, H. Zou, Y. Tan, Y. Xiang, Y. Xu, W. Wu and Y. Zhou, *ChemistrySelect*, 2022, **5**, 8258–8264.
- 27 Z. Pan, L. Qian, J. Shen, J. Huang, Y. Guo and Z. Zhang, *Chem. Eng. J.*, 2021, **426**, 130385.
- 28 H. Hou, Y. Yuan, S. Cao, Y. Yang, X. Ye and W. Yang, *J. Mater. Chem. C*, 2020, **8**, 11001–11007.
- 29 Y. Zhang, Y. Huang, S. S. Zhu, Y. Y. Liu, X. Zhang, J. J. Wang and A. Braun, *Small*, 2021, **17**, 2100320.
- 30 C. Xu, C. Jin, W. Chang, X. Hu, H. Deng, E. Liu and J. Fan, *Catal. Sci. Technol.*, 2019, **9**, 4990–5000.
- 31 X. Fu, H. Yang, H. Sun, G. Lu and J. Wu, *J. Alloys Compd.*, 2016, **662**, 165–172.
- 32 N. Shehzad, M. Tahir, K. Johari, T. Murugesan and M. Hussain, *J. Environ. Chem. Eng.*, 2018, **6**, 6947–6957.
- 33 Z. Xie, Y. Xu, D. Li, S. Meng, M. Chen and D. Jiang, *ACS Appl. Energy Mater.*, 2020, **3**, 12194–12203.
- 34 H. Chai, L. Gao, P. Wang, F. Li, G. Hu and J. Jin, *Appl. Catal., B*, 2022, **305**, 121011.
- 35 X. Zhou, J. Wu, Q. Li, T. Zeng, Z. Ji, P. He, W. Pan, X. Qi, C. Wang and P. Liang, *J. Catal.*, 2017, **355**, 26–39.
- 36 F. Deng, X. Lu, Y. Luo, J. Wang, W. Che, R. Yang, X. Luo, S. Luo and D. D. Dionysiou, *Chem. Eng. J.*, 2019, **361**, 1451–1461.
- 37 X. Lu, W. Che, X. Hu, Y. Wang, A. Zhang, F. Deng, S. Luo and D. D. Dionysiou, *Chem. Eng. J.*, 2019, **356**, 819–829.
- 38 A. Das, M. Patra, M. Kumar P, M. Bhagavathiachari and R. G. Nair, *Mater. Chem. Phys.*, 2021, **263**, 124431.
- 39 M. Lu, Z. Sun, Y. Zhang, Q. Liang, M. Zhou, S. Xu and Z. Li, *Synth. Met.*, 2020, **268**, 116480.
- 40 T. Yang, K. Xue, J. Wang, R. He, R. Sun, U. Omeoga, T. Yang, W. Wang, J. Wang and Y. Hu, *J. Alloys Compd.*, 2020, **818**, 152873.
- 41 F. Guo, W. Shi, M. Li, Y. Shi and H. Wen, *Sep. Purif. Technol.*, 2019, **210**, 608–615.
- 42 W. Ye, J. Hu, X. Hu, W. Zhang, X. Ma and H. Wang, *ChemCatChem*, 2019, **11**, 6372–6383.
- 43 W. Yue, S. Han, R. Peng, W. Shen, H. Geng, F. Wu, S. Tao and M. Wang, *J. Mater. Chem.*, 2010, **20**, 7570–7578.
- 44 J. Park, T. H. Lee, C. Kim, S. A. Lee, M. J. Choi, H. Kim, J. W. Yang, J. Lim and H. W. Jang, *Appl. Catal., B*, 2021, **295**, 120276.
- 45 L. Li, H. Gao, Z. Yi, S. Wang, X. Wu, R. Li and H. Yang, *Colloids Surf., A*, 2022, **644**, 128758.
- 46 Z. Gao, H. Yang, J. Li, L. Kang, L. Wang, J. Wu and S. Guo, *Appl. Catal., B*, 2020, **267**, 118695.
- 47 L. Kang, L. Xu, Z. Han, H. Yu, Q. Wu, M. Wu, Z. He, L. Wang and H. Yang, *Chem. Eng. J.*, 2022, **429**, 132355.
- 48 T. Cheng, H. Gao, G. Liu, Z. Pu, S. Wang, Z. Yi, X. Wu and H. Yang, *Colloids Surf., A*, 2022, **633**, 127918.
- 49 Q. Zhao, Z. Liu, J. Li, W. Yan, J. Ya and X. Wu, *Int. J. Hydrogen Energy*, 2021, **46**, 36113–36123.
- 50 Q. Qiu, P. Zhu, Y. Liu, T. Liang, T. Xie and Y. Lin, *RSC Adv.*, 2021, **11**, 3333–3341.
- 51 Z. He, H. Yang, J. Sunarso, N. H. Wong, Z. Huang, Y. Xia, Y. Wang, J. Su, L. Wang and L. Kang, *Chemosphere*, 2022, **303**, 134973.
- 52 Z. He, Y. Xia, J. Su and B. Tang, *Opt. Mater.*, 2019, **88**, 195–203.
- 53 Z. He, Y. Xia, B. Tang and J. Su, *Mater. Res. Express*, 2017, **4**, 095501.
- 54 X. Wei, C. C. Wang, Y. Li, P. Wang and Q. Wei, *Chemosphere*, 2021, **280**, 130734.
- 55 X. Wang, X. Wang, H. Yang, A. Meng, Z. Li, L. Yang, L. Wang, S. Li, G. Li and J. Huang, *Chem. Eng. J.*, 2022, **431**, 134000.

